Trans Indian Inst Met (2021) 74(7):1663–1672
https://doi.org/10.1007/s12666-021-02256-z

ORIGINAL ARTICLE

Microstructure and Phase Analysis of Multilayer Ni–Cr–Mo Clad for Corrosion Protection

M. Najafi[1] · M. Moshkbar Bakhshayesh[1] · A. Farzadi[1]

Received: 3 January 2021 / Accepted: 5 April 2021 / Published online: 29 April 2021
© The Indian Institute of Metals - IIM 2021

Abstract Ni–Cr–Mo clads are commonly used on carbon steels in the oil and gas industry due to the high resistant corrosion. In this study, a three-layer Ni–Cr–Mo clad was deposited using the GMAW process. The welding current of 200 A, the welding speed of 35 cm/min, and the electrode extension of 20 mm, as well as the torch angle of 25°, are utilized to obtain a low dilution. The results showed that Fe content in the second and third layers of the clad was below 2 wt%. The segregation of Nb and Mo to interdendritic regions contributed to the formation of secondary phases, such as Laves and MC carbide precipitates. The results of chemical analysis across some dendrites and interdendritic regions confirmed that the contents and distribution of secondary phases were insignificant. Also, the transition region where the chemical composition significantly changes to reach the composition of the first layer of the clad is apparent. The microstructure of this region changes from the planar to cellular. The corrosion behavior of the clad was investigated, and it was found that corrosion resistance is not affected when the Fe content is restricted to below 2%. A passive layer consisting of Mo, Nb, Ni and Cr with O is formed on the corroded surface.

✉ A. Farzadi
farzadi@aut.ac.ir

M. Najafi
mehdinajafi@aut.ac.ir

M. Moshkbar Bakhshayesh
m.moshkbar@aut.ac.ir

[1] Department of Materials and Metallurgical Engineering, Amirkabir University of Technology (Tehran Polytechnic), No. 350, Hafez Ave, Valiasr Square, Tehran 15916-34311, Iran

Keywords Dilution · Weld overlay · Carbon steel · Laves phase · Fe content · Segregation

1 Introduction

One of the essential components of oil platforms is the pressure vessel that separates the water from the sour gas to reduce corrosion. This vessel is made of ASTM A516 Gr. 70 and is currently weld cladded by nickel-based alloys. Ni–Cr–Mo alloys such as Inconel 625 are applied on the outer surface of the vessel due to the excellent combination of mechanical properties, high-temperature corrosion/oxidation resistance and weldability. The nickel-based alloys can be strengthened by solid-solution hardening, precipitation hardening or both. Because of the considerable expense of Ni in Inconel alloys, these alloys are not economically feasible to be used as bulk materials and are usually used as welding materials in overlay welding [1, 2].

The process of depositing a layer of a material on the surface of the base metal is called weld overlaying. This process is an attractive way to enhance the corrosion resistance, especially in a harsh environment, instead of manufacturing the whole component from particular materials. The deposited layer and the base metal are mixed in the fusion zone, and a strong metallurgical bond forms between the fusion zone and the base metal. This process can be performed by various welding procedures such as metal inert/active gas (MIG/MAG), tungsten inert gas (TIG), plasma arc welding, and manual metal arc welding (MMAW) [3, 4].

The microstructural characterization and the chemical composition changes of Inconel 625 weld overlay deposited on a boiler steel after annealing at temperatures from 600 to 1000 °C were investigated by Petrzak et al. [5].

According to this study, secondary phases and carbides were precipitated as a result of reactions between alloying elements such as nickel, chromium, titanium, niobium and carbon, depending on the annealing temperature and the selected duration. At 850 °C (1123 K) or higher, the intermetallic compounds such as Laves phase, compounds of Ni and Nb, MC, M_6C, and $M_{23}C_6$ type carbides can form. Redistribution of alloying elements during solidification depends on thermodynamic condition factors and solidification kinetics such as diffusion, undercooling, and fluid flow. The chemical composition heterogeneities limited to micro-regions formed during solidification in non-equilibrium conditions [6]. In this regard, the morphology, distribution and content of Lave phases depend on the microsegregation of Mo and Nb elements [3]. Carvaliho Silva et al. [7] indicated that a complex precipitate, consisting of a TiN core surrounded by (Nb, Ti)C, formed during the solidification process.

The Fe content in the weld overlay is the key element that must be controlled. It is observed that the corrosion properties are not affected when the Fe content is restricted to below 5% [8]. Increasing the dilution level can result in the formation of the deleterious secondary phases. Laves and carbide precipitates reduce the toughness, fatigue strength, and creep rupture strength of the welds [9]. In other words, optimum heat input is necessary not only to decrease the dilution and the segregation level of major alloying elements in the clad but also to provide sufficient wetting [10–12]. Gue et al. [1] indicated that cladding using the hot wire pulsed tungsten inert gas (PTIG) process could enhance corrosion resistance. They also showed that the corrosion resistance of the second layer was close to that of wrought Inconel 625.

In the present work, customized GMAW is used to deposit the three-layer Ni–Cr–Mo clad. The desired welding parameters must be determined to reduce the formation of secondary phases (Laves and carbide precipitates), which is not received much attention in the literature. The low heat input decreases the dilution and the segregation level in the clad. The microstructure and corrosion properties of the clad containing below 5 wt% Fe are studied.

2 Experimental Procedures

A workpiece in size of 300 mm × 200 mm × 20 mm was cut from an ASTM A516 Gr. 70 plate. A three-layer clad was deposited on the workpiece through a gas metal arc welding (GMAW) machine, equipped with a cold wire automatic feeding system. An AWS ERNiCrMo-3 wire electrode with a diameter of 1.25 mm was used. Using optical emission spectroscopy, the chemical composition of ASTM A516 Gr. 70 steel is shown in Table 1. The chemical composition of the consumable electrode wire is also given in Table 1, based on the producer's document.

The welding conditions were adopted from the literature [13, 14] to obtain a shallow and wide weld bead with a lower dilution. Also, some preliminary welding experiments were performed to achieve the desired shape of the weld bead. The relevant welding parameters, which were kept constant for each layer, are given in Table 2. The combination of normal welding current, high welding speed, and high electrode extension, as well as the correct torch angle, are crucial to obtaining a low heat input and dilution. The maximum inter-pass temperature was 250 °C, and as the shielding gas, pure argon was used.

Several cladded samples were cut out of the cladded workpiece using an electrical discharge machine. Then, these samples were conventionally prepared for metallographic analysis, characterization of microstructure, and identification of secondary phases. The clad was electrochemically etched in a 10% aqueous solution of oxalic acid under the voltage of 6 V for 30 s, according to ASTM E407-07 [15]. Also, the clad was chemically etched in a mixture solution (15 ml HCl + 10 ml CH_3COOH + 10 ml HNO_3), and the base metal was subjected to conventional etching with 2% Nital. An OPTICA B-383METT optical microscope (OM) and a MIRA3 TESCAN scanning electron microscope (SEM), equipped with energy-dispersive X-ray spectroscopy (EDS) systems, were applied to carry out the microstructure examinations. The identification of the phases in the clad was carried out using a Philips XPert MPD X-ray diffractometer. Diffraction profiles were recorded using copper radiation at 40 kV in the 2θ angular range 0 to 85° with a step size of 0.02°. Vickers hardness tests, which were repeated at least three times, were performed using a 10 kg load.

A potentiostat/galvanic Autolab® model PGSTAT 302N equipped with Nova 1.9 software was used to test potentiodynamic polarization for evaluating the electrochemical behavior of the Ni–Cr–Mo clad. A conventional three-electrode cell composed of the working electrode, a saturated calomel reference electrode (Ag/AgCl), and a platinum auxiliary (counter) electrode was applied to conduct electrochemical measurement. Prior to applying any potential, the samples were immersed in the test solution for 30 min in order to reach the open-circuit potential (OCP). Afterwards, these samples were polarized from 250 mV below the OCP to 1500 mV above the OCP at the scanning rate of 30 mV min^{-1}. The corrosion potential and corrosion current were calculated using the Tafel extrapolation method. The 3.5 wt% NaCl solution in which these samples were polarized was prepared using an analytical reagent of sodium chloride and distilled water.

Table 1 Chemical composition analyses (wt%) of ASTM A516 Gr. 70 steel and electrode wire

	C	Mn	Si	Ni	Cr	P	S	Al	Mo	Nb	Ti	Fe
Base metal	0.17	1.19	0.32	0.03	0.03	0.019	0.011	< 0.005	< 0.005	< 0.002	< 0.002	Bal
Electrode wire	0.05	≤ 0.50	≤ 0.50	63	21.5	–	–	≤ 0.40	9.00	3.65	≤ 0.40	Bal

Table 2 GMAW welding parameters

Parameters	Conditions
Welding voltage	28 V
Welding current	200 A
Welding speed	35 cm/min
Wire feed rate	8 m/min
Electrode extension	20 mm
Shielding gas flow rate	18 L/min
Torch angle	25 degree
Polarity	DCEP
Heat input	9.6 kJ/cm

3 Results and Discussion

Figure 1 shows the macrograph of the transverse cross section of the clad. This view indicates the good metallurgical bond formed between the fusion zone and the base metal. Also, the entire weld shows no evidence of porosities, cracks, lack of fusion (LOF) and lack of penetration (LOP). This can be attributed to selecting the appropriate welding method and the process parameters. The measured thickness of the clad and the penetration depth are 8 mm and 2.1 mm, respectively. Dilution, the proportion of the base metal in the resultant clad, is about 13%, which can lead to a favorable distribution of Fe in the fusion zone. The chemical composition of the deposited layers, which the third layer is at the top, is given in Table 3. The results indicate that the Fe content is within the acceptable range (below 5 wt%) in the second and third layers of the clad [16].

Figure 2 shows the microstructure of the clad, which is characterized using optical microscopy. According to Fig. 2a, the base metal is low carbon steel with a ferritic–pearlitic microstructure where perlite appears as black. The microstructure of the first layer consists of fine dendrites, owing to the fact that the first layer is deposited onto the base metal with a lower temperature, and the cooling rate and thermal gradient are high. However, the subsequent layers consist of coarse, columnar dendrites (Fig. 2c, d) due to the lower cooling rate and the thermal gradient in this layer.

Fig. 1 Macrostructure of the clad

Figure 3 presents the microstructure adjacent to the base metal–clad interface. As indicated in Fig. 3, the interface is composed of zones of planar, cellular and cellular dendritic growth. The planar region, which occurs at the beginning of solidification, manifests nearly featureless at low magnification. This region is often observed at the fusion boundary and is usually relatively narrow [6, 16–19]. The solidification continues with cellular morphology; then, it quickly breaks down into cellular dendritic growth within some microns of the fusion boundary. The direction of dendrites is the same as the direction of heat transfer during solidification.

Figure 4a shows an electron microscope image of the microstructure adjacent to the fusion boundary. In addition to the base metal (region A), three distinct regions can be identified in the weld metal. Region B is immediately adjacent to the fusion boundary (base metal), and no grain boundary is observed in this region. Region C is at the top of region B and indicates cellular growth. Finally, region D is the furthest region from the fusion boundary. The results of the EDS analysis for these regions are presented in Fig. 4b. The chemical composition in region D is roughly equal to that in the first layer of the clad (Table 3).

Thus, the base metal and the filler metal were mixed in region D, which is called the composite region. From the base metal to the composite region (D), the Cr, Ni and Fe contents vary greatly, as the dissimilar filler metal is deposited. The content of Fe decreases, while the concentrations of Ni and Cr sharply increase from approximately zero to about 50 wt% Ni and 18 wt% Cr, respectively. In fact, the chemical composition changes across the weld metal until it reaches the composition of the first layer of the clad. Hence, regions B and C create the transition region. The width of the transition region depends on solidification conditions and welding methods [6, 16–19]. In this case, the width of this region is about 25 microns. It

Table 3 Chemical composition (wt%) of the clad, layer by layer

	C	Cr	Mo	Nb	Fe	Ti	Si	Mn	S	V	Ni
First layer	0.026	20.82	8.89	3.27	5.23	0.22	0.19	0.1	< 0.005	0.014	Bal
Second layer	0.021	20.91	9.12	3.41	0.9	0.24	0.21	0.05	< 0.003	0.016	Bal
Third layer	0.02	21.87	8.82	3.28	1.51	0.23	0.2	0.05	< 0.003	0.014	Bal

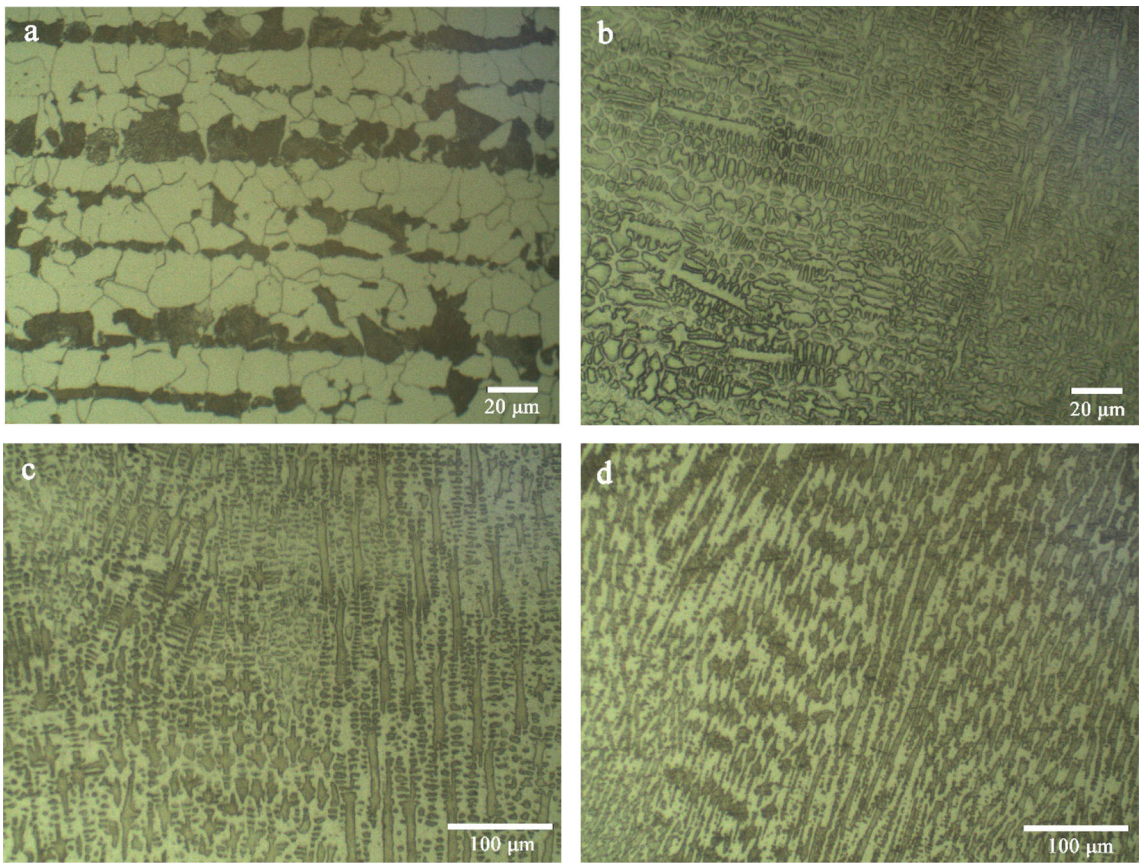

Fig. 2 Optical micrographs of microstructure in **a** base metal, and **b** first layer, **c** second layer, and **d** third layer of clad, after electroetching in 10 wt% aqueous solution of oxalic acid for 30 s

is interesting that the solidification microstructure changes from the planar to cellular in the transition region. If the dilution of Ni-based filler metal and the base metal is very high, martensite can form within the transition region close to the fusion boundary; the presence of martensite causes hydrogen-induced cracking (HIC) [17, 19].

Figure 5a shows dendrite arms and interdendritic regions with the reference line perpendicular to the dendrite arms. Also, some secondary phases with irregular shapes and a cuboidal morphology are observed in the interdendritic regions. In order to assess microsegregation, the chemical analysis is carried out along the line. The line was 13 microns long, and the measurements were spaced every 0.7 microns. Figure 5b shows the variations in the content of Cr, Fe, Nb and Ti along the line. The interdendritic regions, specified with arrows, are enriched with Nb, while the dendrite cores are rich in Fe and Cr. Apart from the secondary phases, the distribution of Ti is considerably uniform in the microstructure. Furthermore, the Nb content in the secondary phases is higher than in the interdendritic regions where the secondary phases are not observed. The distribution of solute elements during the solidification of nickel-based alloys depends on the partition coefficient, k, indicating the intensity and direction of microsegregation [6, 7, 16, 20]. If $k > 1$, the concentration of the solute element in the solid phase is higher than in the liquid one solidifying at the end. However, $k < 1$ means that the solute element segregates to the interdendritic regions. Carvaliho Silva et al. [7] calculated the k values for Cr, Nb, Mo and Fe, which are equal to $k_{Ni} = 1.04$;

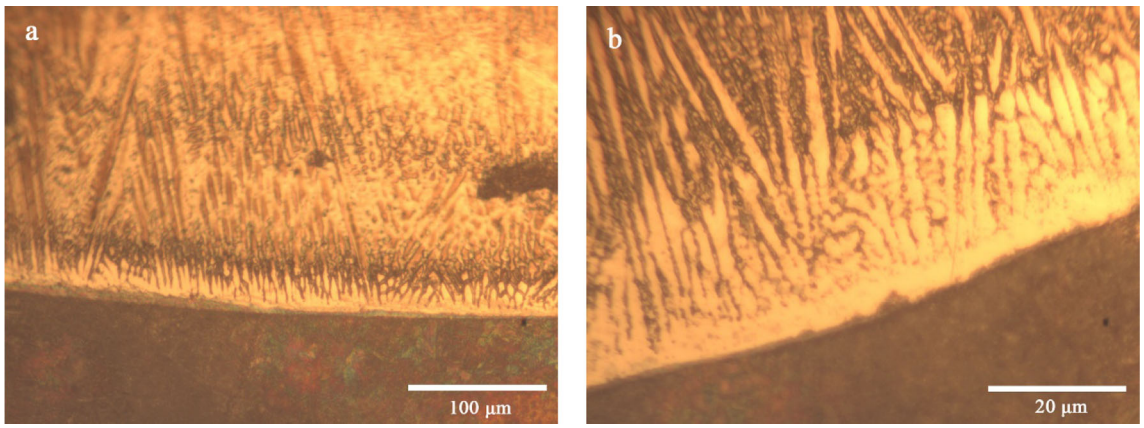

Fig. 3 **a** Optical images of the base metal–clad interface showing distinct regions. **b** Enlarged image showing planar, cellular and cellular dendritic growth

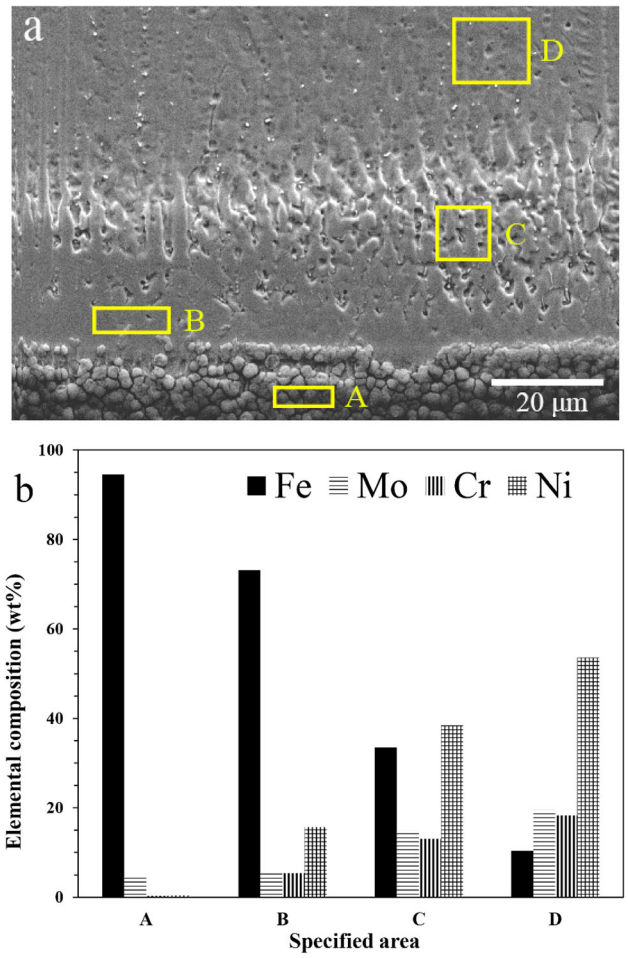

Fig. 4 Base metal–clad interface regions; **a** scanning electron microscopy showing the region in detail. **b** The quantitative analysis of specified areas, B and C are in the transition zone

$k_{Cr} = 1.05$; $k_{Nb} = 0.49$; $k_{Mo} = 0.89$; $k_{Fe} = 1.14$. Consequently, Nb has the strongest tendency to segregate during solidification. These calculations are consistent with the

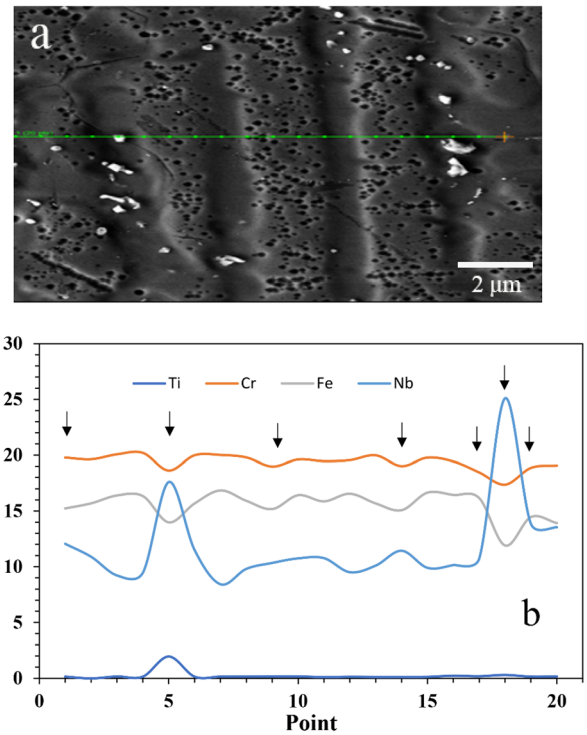

Fig. 5 **a** SEM image of the microstructure of the clad indicating some dendrite arms, **b** line profile showing the elemental segregation from the dendrites to the interdendritic regions during the solidification process. The arrows indicate the interdendritic regions

diagram in Fig. 5b. Nb and Mo, which have lower partition coefficients than the other elements, mainly contribute to the formation of the secondary phases. In this regard, increasing the dilution level and the Fe concentration in the weld metal aggravate microsegregation of Mo and Nb through a decrease in their k values [7, 16]. Welding parameters such as heat input and filler metal feed rate have effects on the weld quality and the microstructure, and these parameters can change segregation potential and

dilution [21–23]. As shown in Fig. 5b, the amounts of the secondary phases in this work are insignificant since the element contents have a virtually constant trend along the scan line. This microstructure reduces the susceptibility of the clad to solidification cracking due to a decrease in both Nb segregations and detrimental secondary phases, and hence it can improve mechanical properties such as ductility and toughness [21, 24]. If a higher heat input were applied in the present study, an increase in the amount of the secondary phases would be expected.

The first secondary phase, which is observed in Fig. 5a, is shown in Fig. 6. This type of the secondary phase has a eutectic morphology with an elongated form or rod-shaped, and it typically forms in the interdendritic regions. SEM–EDS analysis indicates that this phase is enriched with Nb and Mo (Table 4). Given the chemical composition and the morphology, this is Laves phase, in the form of $(Ni, Cr)_2(Nb, Mo, Si)$ with a hexagonally close-packed crystallographic structure [25]. The segregation of Nb and Mo to the interdendritic regions makes the microstructure prone to form Laves. Laves is a brittle intermetallic phase and acts as a preferential site for crack initiation and propagation.

The X-ray diffraction (XRD) pattern of the clad is shown in Fig. 7. Only peaks of the Ni matrix (γ) are identified. This pattern confirms that the volume fraction of the secondary phases is small and insignificant. In comparison with the theoretical positions of pure nickel, all peaks are shifted in the direction of higher values of the angle θ, due to the presence of alloy elements that change the parameter of the solid solution crystal structure.

The other type of the secondary phase with a cubic morphology is shown in Fig. 8a. The chemical EDS maps of this phase, which are presented in Fig. 8b–g, indicate that it is rich in Nb, C and Ti; consequently, the phase could be a MC carbide consisting of Nb and Ti ((NbTi)C) [6, 7, 16, 17]. During solidification, the dendrites of austenite (γ), which form at the beginning of solidification, grow and reject Mo, Nb and C to the liquid in the interdendritic regions ($L \rightarrow \gamma$). These elements regularly accumulate in these regions, and hence the MC carbides form by the eutectic reaction $L \rightarrow \gamma + \text{MC}$. Carbon, which could suppress the formation of Laves phase, is consumed during the reaction. Finally, the solidification process is finished through the eutectic reaction $L \rightarrow \gamma +$ Laves phase [1, 7, 20]. The formation of these secondary phases during welding is highly dependent on the chemical composition of the weld metal.

The hardness values of the base metal, HAZ and the clad are shown in Fig. 9. The hardness increases from the base metal to the clad. The hardness of the HAZ is higher than the hardness of the base metal, i.e. 216 HV and 156 HV, due to the formation of the bainitic microstructure in the HAZ. The low heat input of welding causes faster cooling, which is the reason for the formation of the bainite. The hardness values for the layers of the clad are in the range of 218 to 238 HV. These values are below 250 HV and acceptable, according to NACE MR0175 [26]. Additionally, there is a correlation between the hardness and the strength of the clad.

The potentiodynamic polarization curves of the base metal and the clad in 3.5% NaCl solution are shown in Fig. 10. The corrosion potential (E_{corr}), passive current density (I_p) and the corrosion current (I_{corr}) are calculated using the Tafel extrapolation from the potentiodynamic polarization curves, and the corresponding parameters are shown in Table 5. The base metal has a lower E_{corr} than the clad, which indicates that the base metal requires a smaller driving force to initiate corrosion. This means that the Ni–Cr–Mo clad presents excellent resistance in a corrosive environment. The formation of a passive protective film at low current density on a metal surface is considered to be a positive characteristic to prevent extreme corrosion at higher current densities. As illustrated in Fig. 10a, the

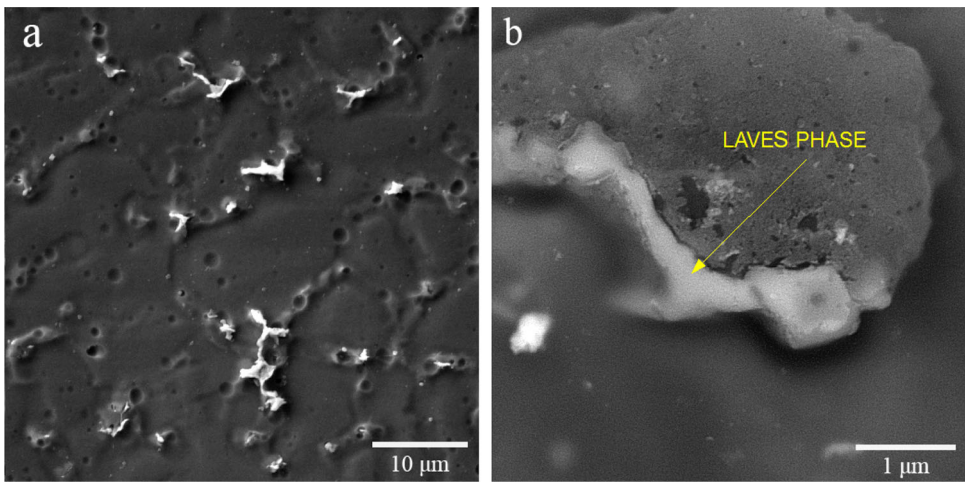

Fig. 6 **a** Lave phases formed along interdendritic regions, **b** enlarged image of Laves phase

Table 4 Elemental composition (SEM–EDS) of Laves phase (in wt%) shown in Fig. 6

Si	Cr	Mo	Ni	Nb
1.39	13.9	22.0	39.4	23.3

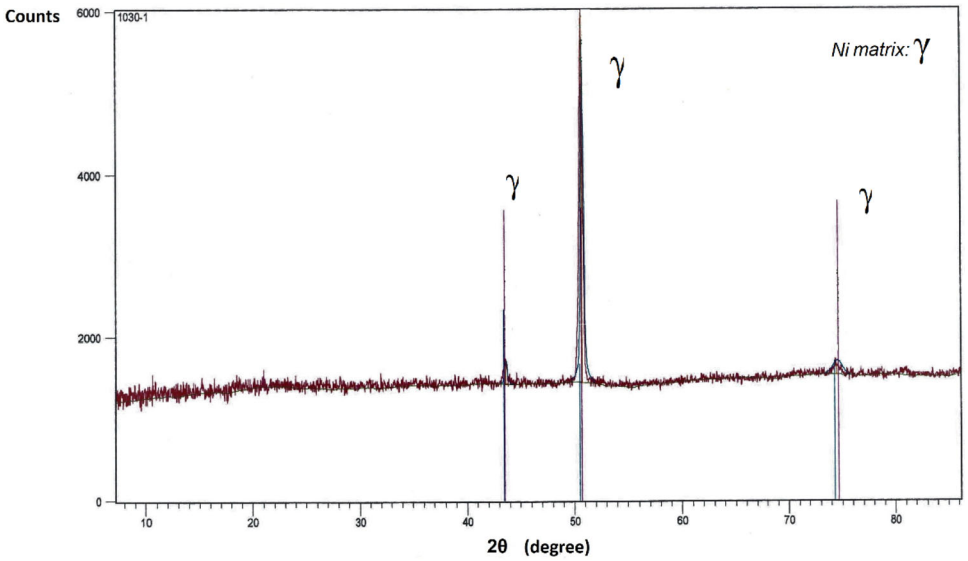

Fig. 7 X-ray pattern of the Inconel 625 weld overlay, showing insignificant content of the secondary phases

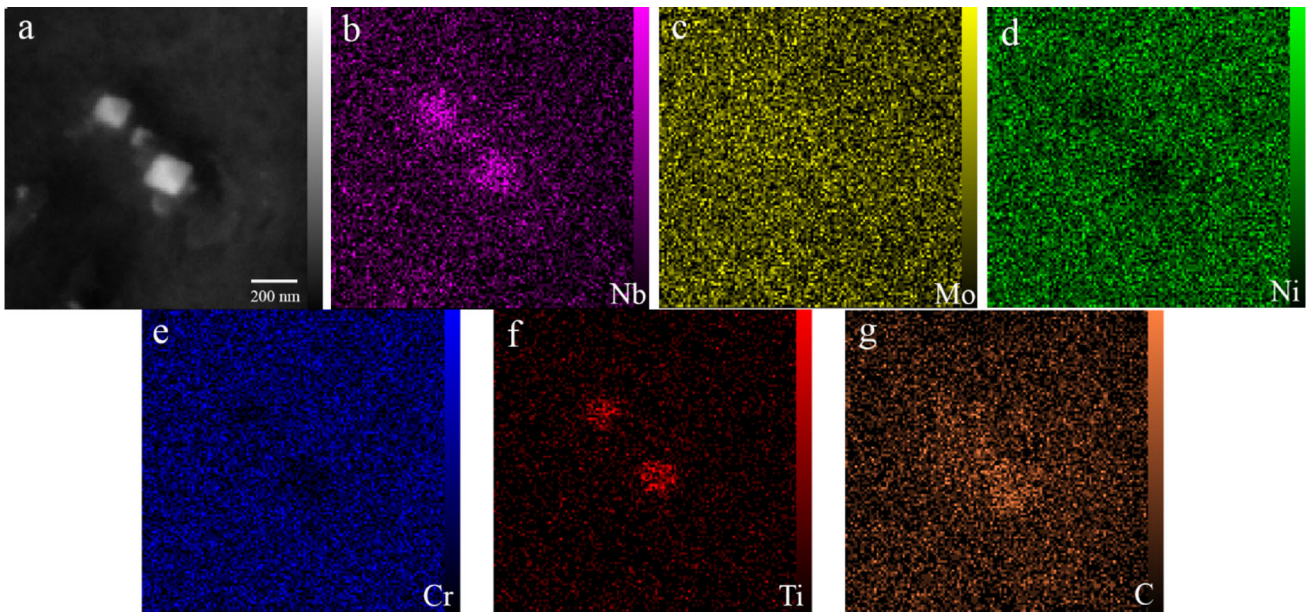

Fig. 8 **a** Scanning electron microscope micrograph showing the main morphologies of secondary phases observed into the weld metal. The elemental chemical maps obtained by energy dispersive X-ray spectroscopy for: **b** Nb; **c** Mo; **d** Ni; **e** Cr; **f** Ti; **g** C

anodic current density gradually increases when the potential changes in upright direction and hence the base metal indicates an active dissolution behavior. However, the clad presents a stable and wide passive region due to the high chromium content, as shown in Fig. 10b. Moreover, in the transpassive region, the rate at which the current density increases against the potential is low. Thus, permanent damage cannot form on the passive layer. The corroded surface of the clad is observed by SEM, as shown in Fig. 11. The observations demonstrate that there is no pitting corrosion, and corrosion damage is uniform. It is

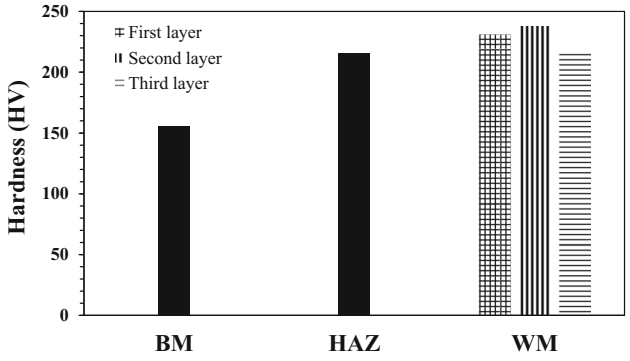

Fig. 9 Values of hardness obtained from different zones

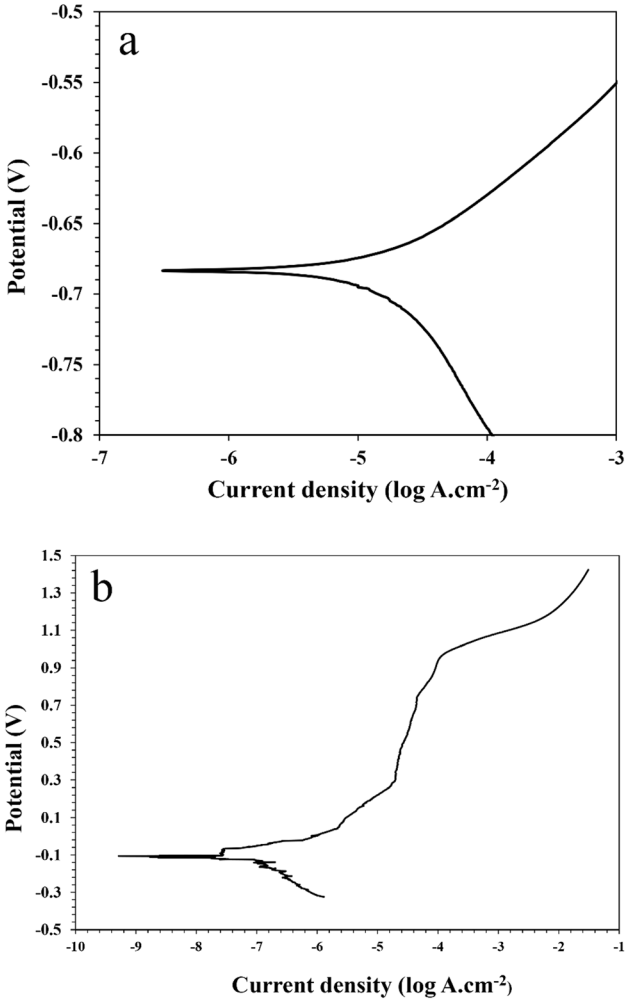

Fig. 10 Polarization curves of **a** the base metal and **b** the clad

also found that restricted Fe content does not affect the corrosion resistance of the clad.

The SEM–EDS elemental maps of the corroded clad are shown in Fig. 12. Despite the intermetallic compounds and secondary phases, the passive layer forms on the Ni-based matrix. The corrosion products (the passive layer), which form on the clad surface after potentiodynamic test, mainly consist of Mo and Nb with O. In addition to Mo and Nb, Ni and Cr are also present in the corrosion products.

4 Conclusions

In the present work, the microstructure of the Ni–Cr–Mo clad deposited by gas metal arc welding was studied. Also, the corrosion behavior of the clad was investigated using potentiodynamic polarization and Tafel extrapolation method. The main results are listed below.

(1) GMAW process parameters are adjusted to obtain minimum heat input and minimum dilution. Hence, normal welding current (200 A), high welding speed (35 cm/min), and high electrode extension (20 mm), as well as correct torch angle (25°), are used. Macrostructure studies corroborate enough penetration between the base metal and the clad with the absence of welding defects such as porosity, and surface crack.

(2) The microstructure of the first layer consists of fine dendrites, and the microstructure of the upper layers consists of coarse, columnar dendrites. In addition, the microstructure adjacent to the fusion boundary is composed of planar, cellular and cellular dendritic. From the base metal to the composite region, the chemical composition significantly changes until it reaches the composition of the first layer of the clad. Hence, the transition region is apparent. The microstructure of this region changes from the planar to cellular.

(3) While Ni–Cr–Mo clad is a solid solution strengthened alloy, the negligible distribution of Nb- and Mo-rich secondary phases such as Laves and MC carbides ((NbTi)C) is found in the interdendritic regions. The segregation of Nb and Mo to the interdendritic regions makes the microstructure prone to form Laves and these carbides. Increasing the dilution level and the Fe concentration in the weld metal aggravate microsegregation of Mo and Nb through a decrease in their k values.

(4) The conducted corrosion experiments in the 3.5 wt% NaCl solution exhibit that the corrosion potential (E_{corr}) sees an increase from − 0.683 V in the base to − 0.106 V in the clad. As a result, the clad has more corrosion resistance compared with the base metal. The passive film on the clad surface is stable. A passive layer consisting of Mo, Nb, Ni and Cr with O is formed during corrosion. Additionally, the corrosion resistance of the clad does not affect if the Fe content is below 2%.

Table 5 Corresponding corrosion parameters obtained from the polarization curves

Sample	E_{corr} (V)	I_{corr} (A/cm^2 × 10^{-7})	I_p (A/cm^2 × 10^{-5})
Base metal	− 0.683	162	–
Ni–Cr–Mo clad	− 0.106	1.53	1.88

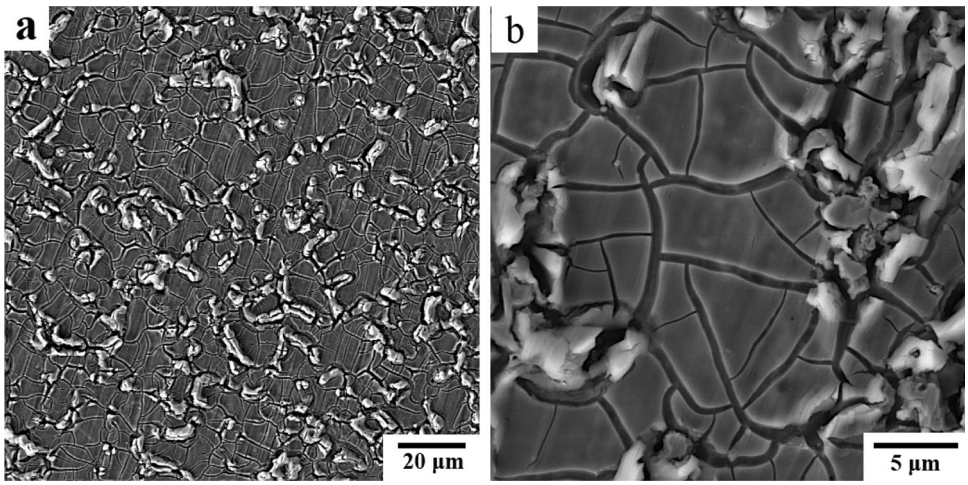

Fig. 11 **a** Scanning electron micrograph of a corroded surface of clad after potentiodynamic test, **b** enlarged image

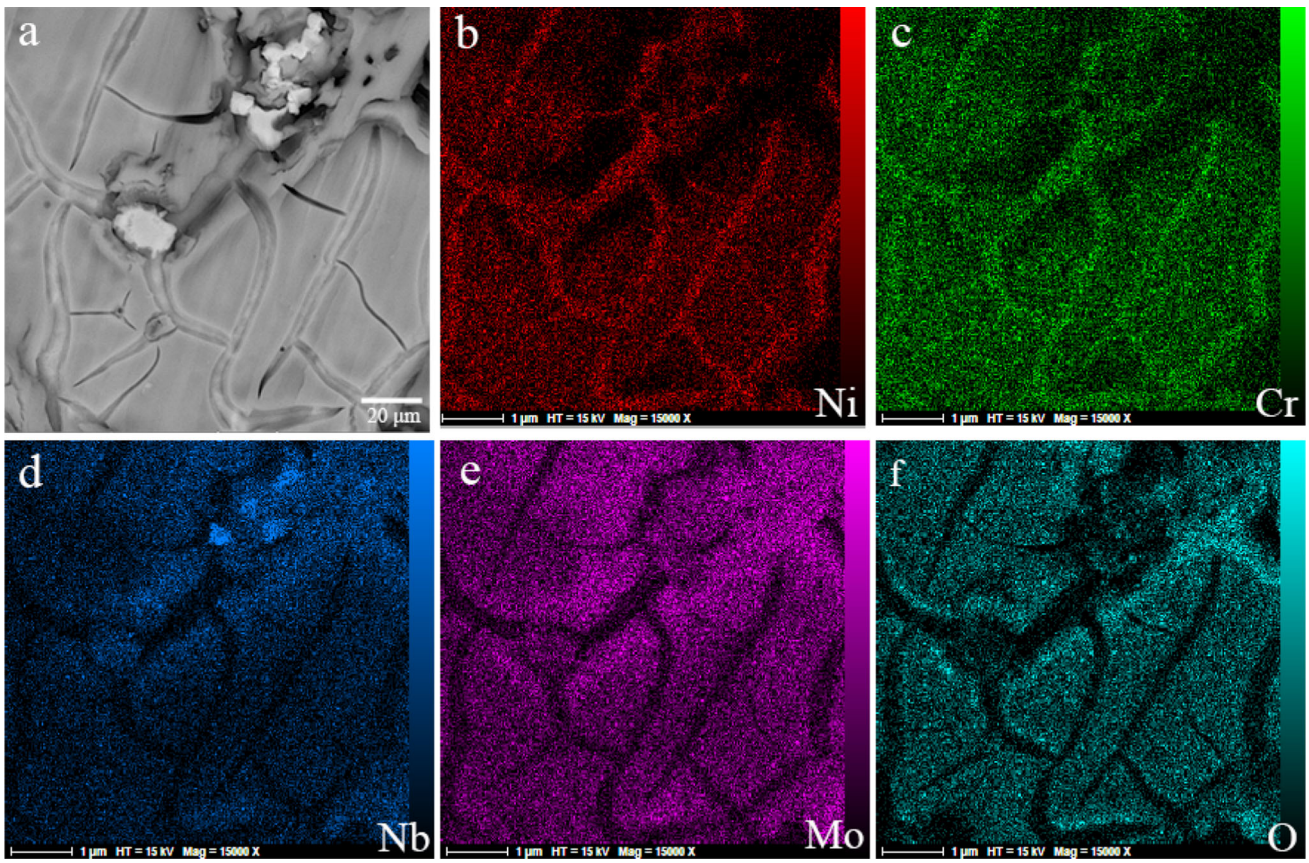

Fig. 12 **a** Scanning electron microscope micrograph showing the corrosion products and elemental maps for **b** Ni, **c** Cr, **d** Nb, **e** Mo, and **f** O

References

[1] Guo L, Zheng H, Liu S, Li Y, Feng C, and Xu X, *Int J Electrochem Sci* **11** (2016) 5507.
[2] Cuevas-Arteagaa C, Verhelstb D, and Alfantazia A, *ECS Trans* **28** (2010) 61.
[3] Xing X, Xinjie D, and Baosen W, *J Alloys Compd* **593** (2014) 110.
[4] Lippold J C, Kiser S D, and DuPont J N, *Welding Metallurgy and Weldability of Nickel-Base Alloys*, 1st edn, John Wiley & Sons Inc, New York (2011).
[5] Petrzak P, Kowalski K, and Blicharski M, *Acta Phys Pol A* **130** (2016) 1041.
[6] Razmus-Gornikowska M, and Blicharski M, *Arch Metall Mater* **60** (2015) 2599.
[7] Silva C C, Miranda H C, Motta M F, Farias J P, Afonso C R M, and Ramirez A J, *J Mater Res Technol 2* (2013) 228.
[8] Elango P, Balaguru S, *Indian J Sci Technol* **8** (2015) 1.
[9] Ban S, Shin Y T, Lee S R, and Lee H, *Int J Electrochem Sci* **11** (2016) 7764.
[10] Jung E, and Lee H, *Int J Electrochem Sci* **11** (2016) 7125.
[11] Kalivodova J, Baxter D, Schutze M, and Rohr V, *Mater Corros* **59** (2008) 367.
[12] Banovic S W, Dupont I N, and Marder A, *Metall Mater Trans B* **32** (2001) 1171.
[13] Shihab S K, Mohamed R M, and Mubarek E M, *Mater Today Proc* **16** (2019) 816.
[14] Palani P K, and Murugan N, *Int J Adv Manuf Technol* **30** (2006) 669.
[15] ASTM E407-07, Standard Practice for Microetching Metals and Alloys, ASTM International, Pennsylvania (2015).
[16] Razmus-Gornikowska M, Cieniek L, Blicharski M, and Kusinski J, *Arch Metall Mater* **59** (2014) 1081.
[17] Razmus-Gornikowska M, and Blicharski M, *Arch Metall Mater* **62** (2017) 787.
[18] Araujo A A D, Bastian F L, and Castrodeza E M, *Fatigue Fract Eng Mater Struct* **39** (2016) 1477.
[19] Alexandrov B T, Lippold J C, Sowards J W, Hope A T, and Saltzmann D R, *Weld World* **57** (2013) 39.
[20] Sandes S S, Alvaraes C P, Mendes M C, Araujo L S D, Souza L F G D, and Jorge J C F, *Weld Int* **32** (2017) 179.
[21] Zahran E M, and Alfantazi A M, *Metall Mater Trans A* **44** (2013) 4671.
[22] Dupont J N, Banovic S W, and Marder A R, *Weld J* **82** (2003) 125.
[23] Petrzak P, Blicharski M, Dymek S, and Solecka M, *Solid State Phenom 231* (2015) 113.
[24] Kim J S, and Lee H, *Metall Mater Trans A* **47** (2016) 6109.
[25] Radhakrishna C H, and Rao K P, *J Mater Sci* **32** (1997) 1977.
[26] International Standard NACE MR0175/ISO 15156, Petroleum and Natural Gas Industries Materials for Use in H2S-Containing Environments in Oil and Gas Production, NACE International, Houston (2003).

Publisher's Note Springer Nature remains neutral with regard to jurisdictional claims in published maps and institutional affiliations.